Anisotropic magnetic structures of the MnRMnSbO$_6$ high-pressure doubly ordered perovskites (R = La, Pr, and Nd)

Elena Solana-Madruga,[1,*] Ángel M. Arévalo-López,[2] Antonio J. Dos santos-García,[3] Clemens Ritter,[4] Concepción Cascales,[5] Regino Sáez-Puche,[6] and J. Paul Attfield[1]

[1]*Centre for Science at Extreme Conditions (CSEC) and School of Chemistry, University of Edinburgh, Edinburgh EH9 3JZ, United Kingdom*
[2]*Université de Lille, CNRS, Centrale Lille, ENSCL, Université d'Artois, UMR 8181 - UCCS - Unité de Catalyse et Chimie du Solide, F-59000 Lille, France*
[3]*Departamento de Ingeniería mecánica, Química y Diseño Industrial, ETSIDI, Universidad Politécnica de Madrid, 28012 Madrid, Spain*
[4]*Institut Laue-Langevin, 38042 Grenoble Cedex, France*
[5]*Instituto de Ciencia de Materiales de Madrid, Consejo Suprior de Investigaciones Científicas, c/ Sor Juana Inés de la Cruz 3, 28049 Madrid, Spain*
[6]*Departamento de Química Inorgánica, Facultad de Ciencias Químicas, Universidad Complutense de Madrid, 28040 Madrid, Spain*

(Received 11 January 2018; revised manuscript received 1 March 2018; published 11 April 2018)

A new type of doubly ordered perovskite (also reported as double double perovskite, DDPv) structure combining columnar and rock-salt orders of the cations at the A and B sites, respectively, was recently found at high pressure for MnRMnSbO$_6$ (R = La–Sm). Here we report further magnetic structures of these compounds. Mn^{2+} spins align into antiparallel ferromagnetic sublattices along the x axis for MnLaMnSbO$_6$, while the magnetic anisotropy of Pr^{3+} magnetic moments induces their preferential order along the z direction for MnPrMnSbO$_6$. The magnetic structure of MnNdMnSbO$_6$ was reported to show a spin-reorientation transition of Mn^{2+} spins from the z axis towards the x axis driven by the ordering of Nd^{3+} magnetic moments. The crystal-field parameters for Pr^{3+} and Nd^{3+} at the $4e$ C_2 site of their DDPv structure have been semiempirically estimated and used to derive their energy levels and associated wave functions. The results demonstrate that the spin-reorientation transition in MnNdMnSbO$_6$ arises as a consequence of the crystal-field-induced magnetic anisotropy of Nd^{3+}.

DOI: 10.1103/PhysRevB.97.134408

I. INTRODUCTION

The size and charge mismatches between different transition-metal cations are commonly used as a strategy in the synthesis of ordered ABO_3 perovskite oxides. Among the B-site ordered $A_2BB'O_6$ double perovskites, the $Mn_2MM'O_6$ family has attracted particular interest in recent years due to their magnetic and electric properties. The stabilization of the small Mn^{2+} at the highly coordinated A site of the perovskite structure requires high pressures, while the use of moderate-pressure and high-temperature conditions yields ordered corundum derivative structures, e.g., $LiNbO_3$, Ni_3TeO_6, and ilmenite type. The interest of these moderate-pressure phases lies in the combination of their high-temperature magnetic transitions [1–5] and exotic magnetic behaviors [6] with their expected spontaneous net polarizations, which makes these compounds potential multiferroic materials. In this context, the ilmenite-type Mn_2FeSbO_6 is notable for showing a large magnetoelectric coupling through a nonlinear mechanism at 260 K [7]. Concerning the ordered perovskite-derived polymorphs, only a few $Mn_2MM'O_6$ have been isolated; for instance, the first transition-metal-only double perovskite Mn_2FeReO_6, which shows spin-reorientation transitions and switching of magnetoresistance with temperature [8,9], and Mn_2MnReO_6, where a strong magnetic frustration stabilizes perpendicular spin sublattices [10,11]. It is notable that the use of Sb^{5+} as the M' cation stabilizes both the corundum-derived and the double perovskite polymorphs of the related Mn_2MSbO_6 (M = Cr, Fe, Sc) [6,7,12–15].

The combination of simultaneous 1:1 cation orders at both the A and B sites [16] to give a $AA'BB'O_6$ double double perovskite (DDPv) structure is rare, but was previously reported for the combination of layered A-site and rock-salt B-site orders, e.g., in $NaTbMnWO_6$ [17] and $NaLaMgWO_6$ [18]. A new DDPv type was recently discovered for MnRMnSbO$_6$ (R = La–Sm) [19]. The difference in the ionic radius between large rare-earth cations and Mn^{2+} leads to their order at the A sites in a columnar arrangement. The B sites are occupied by Mn^{2+} and Sb^{5+} ordered in a rock-salt manner. Magnetic susceptibility (0.1 T FC-ZFC data) and magnetization loops at 2 K (scanned from 0 T towards positive values, reversed towards negative values, and switched back to 0 T) were reported in Ref. [19] and are further discussed below. They show the antiferromagnetic (AFM) order of Mn^{2+} spins below $T_N \sim 48$ K for MnLaMnSbO$_6$ and the ferrimagnetic behavior of MnPrMnSbO$_6$ below $T_N \sim 75$ K (see Fig. 1). A more complex magnetic behavior including subsequent χ vs T transitions and a spin-reorientation transition of the Mn^{2+} sublattices from the z towards the x axis, associated with additional order of Nd^{3+} magnetic moments, was observed in MnNdMnSbO$_6$ at low temperatures [19].

Here we report the magnetic structures of MnRMnSbO$_6$ for R = La and Pr. It is well known that the magnetic anisotropy of the R^{3+} cations often influences the magnetic properties and structures of mixed rare-earth transition-metal compounds

*Corresponding author: E.Solana@ed.ac.uk

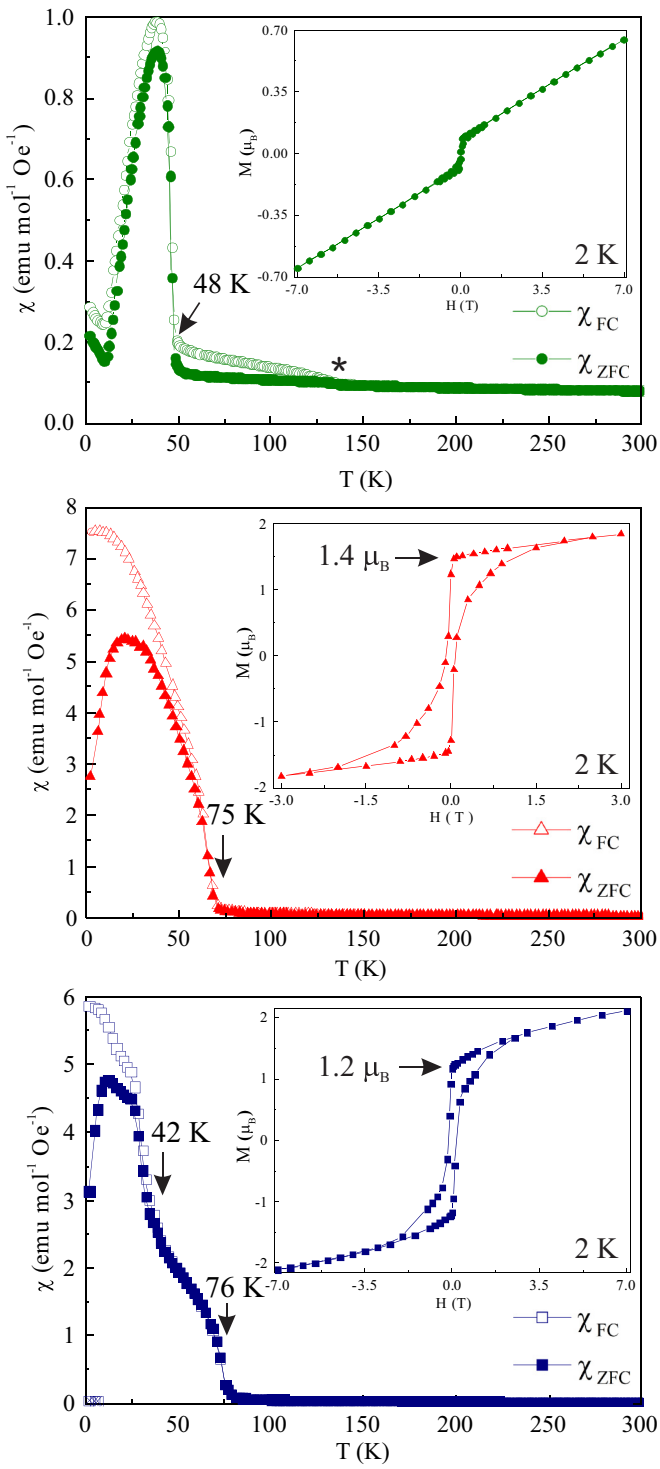

FIG. 1. Experimental magnetic susceptibility and field-dependent magnetization loops at 2 K (insets) of MnRMnSbO$_6$ DDPvs, R = La (top), Pr (middle), and Nd (bottom). The asterisk in MnLaMnSbO$_6$ shows the magnetic transition of the secondary MnO minor phase.

[20] and that this effect usually depends on the strength of the magnetic d-f exchange [21–25]. Therefore, here we also develop a comparative study of the magnetic structures of MnRMnSbO$_6$ (R = La, Pr, and Nd) in terms of the intrinsic and crystal-field-induced magnetic anisotropies of the R^{3+} cations. This relation explains the origin of the three different magnetic behaviors observed in these compounds.

II. EXPERIMENT

MnRMnSbO$_6$ DDPvs were synthesized at 10 GPa and 1473 K using a Walker-type multianvil press, as detailed in [19]. Neutron powder diffraction (NPD) data were collected for ~50 mg samples of MnRMnSbO$_6$ (R = La and Pr) using the high-intensity powder diffractometer D20 instrument at the Institut Laue-Langevin (Grenoble, France) using a wavelength of $\lambda = 2.4$ Å. Long scans were taken at 80 and 1.7 K in the $0 < 2\theta < 130°$ angular range with a 0.1° step size. Additional short scans were collected every 2 K for the Pr-containing compound to study the thermal evolution of its magnetic structure and to compare it to that of the isostructural MnNdMnSbO$_6$. The magnetic symmetry analysis was performed using BASIREPS [26] (see the Supplemental Material [27] for further details) and the diffraction patterns were fitted through the Rietveld method using the FULLPROF package [28].

The calculation of the energy levels of $4f^n (n = 2,3)$ configurations of Pr^{3+} and Nd^{3+} in the DDPv structure considered a total Hamiltonian combining the free-ion (FI) or intraionic interactions (H_{FI}) with the crystal-field (CF) effects (H_{CF}) arising from the influence of the surrounding charges on the $4f^n$ electrons. The expressions for H_{FI} and H_{CF} and those for their involved interactions are detailed in Ref. [29].

For a given R, the FI parameters do not vary much in different hosts. Therefore, these parameters have been taken from the literature for the current modeling [30,31]. In contrast, the CF parameters show a large variation depending on the crystalline environment. Consequently, we have applied the semiempirical simple overlap model (SOM) [32] to generate a set of CF parameters (CFPs) from the crystallographic data of MnPrMnSbO$_6$ and MnNdMnSbO$_6$ compounds, where the symmetry of the 4e site occupied by R is C$_2$, with the binary axis along the [001] direction. The resulting CFPs are summarized in Table S1 of the Supplemental Material (SM) [27].

The subsequent calculation of energy levels, i.e., 91 for Pr and 182 Kramers doublets for Nd, has been carried out using the program IMAGE [33]. For MnNdMnSbO$_6$, anisotropic g values (g_x, g_y, g_z) have also been derived for levels with energy below 5000 cm^{-1}, i.e., $^4I_{9/2}$, $^4I_{11/2}$, and $^4I_{13/2}$, and results are shown in Table S2 of the SM [27].

III. RESULTS AND DISCUSSION

A. Neutron diffraction

The Rietveld fits of the NPD data taken above T_N confirmed the DDPv structure of MnRMnSbO$_6$ (R = La and Pr) with space group $P4_2/n$. The resulting structural details arising from these fits are summarized in Table S3 of the SM [27]. Minor amounts of secondary MnO (7% and 5% wt., respectively) but no signs of RMnO$_3$ (<3% wt. from synchrotron x-ray diffraction in Ref. [19]) could be observed from NPD. Refining the occupancy of oxygen sites does not give any deficiency, which points to the presence of imperceptible amounts of secondary RMnO$_3$ and Sb$_2$O$_4$, usually formed in the related Mn$_2M$SbO$_6$ double perovskites.

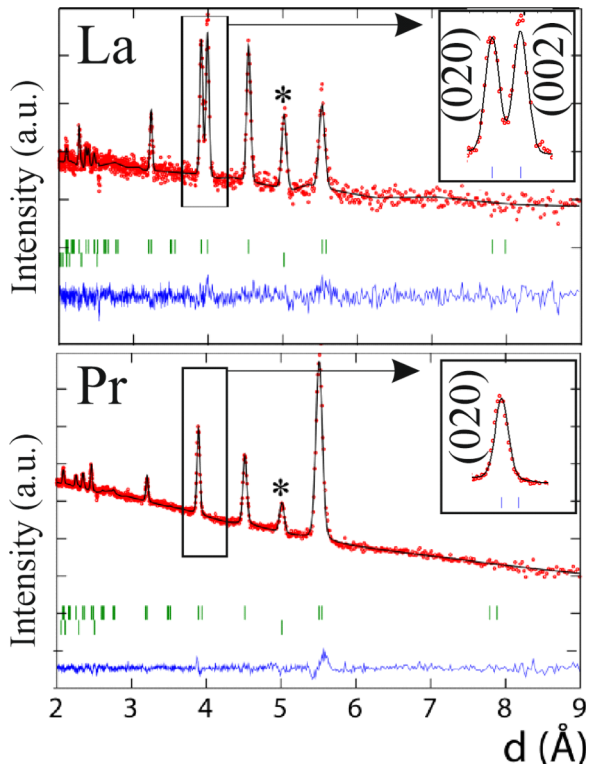

FIG. 2. Rietveld fits to the 1.5–80 K NPD difference patterns showing magnetic peaks for MnRMnSbO$_6$, R = La (top) and R = Pr (bottom). The (020) and (002) peaks are enlarged as insets. The asterisk identifies the MnO magnetic impurity.

Figure 2 shows the fit of the difference pattern obtained by subtracting the profiles collected at 80 K (well above T_N; see Fig. 1) from those collected at 1.5 K for MnLaMnSbO$_6$ (top) and MnPrMnSbO$_6$ (bottom). Subtraction of the nuclear contribution determined at 80 K from the 1.5 K data leaves the magnetic peaks in the difference patterns. Except for the main magnetic peak arising from the secondary MnO (identified with an asterisk in the figure), all the peaks in these patterns could be assigned to the main MnRMnSbO$_6$ phase indexed by the propagation vector $\kappa = [0\,0\,0]$. The most notable difference observed in the patterns is the presence of magnetic (020) and (002) peaks for R = La, but only a single (020) reflection for R = Pr in the $3.85 < d < 4.05$ Å region. This difference evidences that these two compounds develop different magnetic structures. Comparing the labeled magnetic peaks with those reported for MnNdMnSbO$_6$, the magnetic structures of MnRMnSbO$_6$, with R = La and Pr, are expected, and confirmed below, to be similar to those of R = Nd at low temperature and above the spin-reorientation transition temperature, respectively. As further discussed in Sec. III B, the origin of the different magnetic structures of these three compounds is their different magnetic anisotropies: the absence of any paramagnetic R^{3+} cation induces the intrinsic DDPv magnetic structure to MnLaMnSbO$_6$, while the magnetic anisotropy of Pr^{3+} and Nd^{3+} originates a different magnetic structure for MnRMnSbO$_6$ (R = Pr and Nd). The rotation of magnetic moments in MnNdMnSbO$_6$ at low temperature is demonstrated here to arise as a response to the crystal-field-induced magnetic anisotropy.

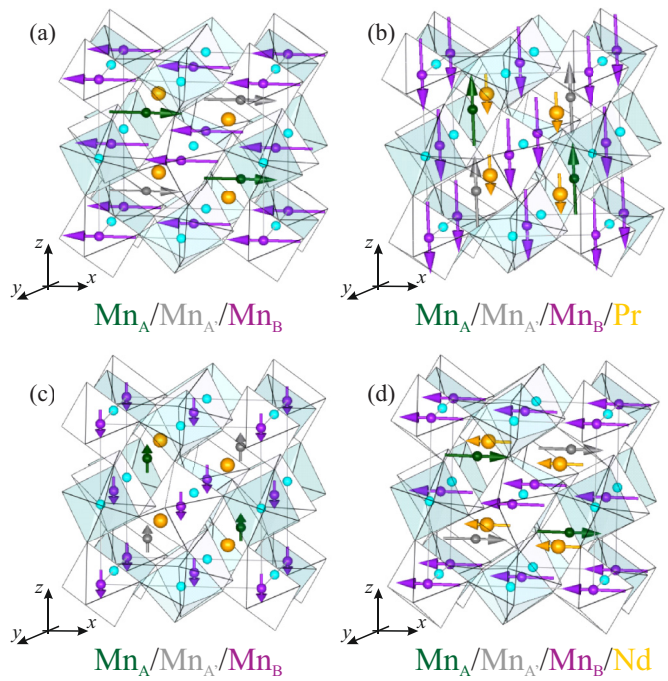

FIG. 3. Magnetic structures of (a) MnLaMnSbO$_6$ and (b) MnPrMnSbO$_6$ at 1.5 K. Those of MnNdMnSbO$_6$ at (c) 60 K and (d) 1.5 K are shown for comparison.

Magnetic symmetry analysis was performed to determine the allowed irreducible representations (IRs) and their basis vectors (BVs) for the Wyckoff $2a$ (Mn$_A$), $2b$ (Mn$_{A'}$), $4c$ (Mn$_B$) and $4e$ (R) positions in space group $P4_2/n$ and for the magnetic propagation vector $\kappa = [0\,0\,0]$. Tables S4–S6 of the SM [27] display the resulting allowed IRs.

Mn^{2+} spins align along the x axis for MnLaMnSbO$_6$, following BV 1 of IR Γ_3 in Table S4 (Mn$_A$/Mn$_{A'}$) and BVs 1+5 of Γ_3 of Table S5 (Mn$_B$) of the SM [27]. In the resulting collinear AFM structure, depicted in Fig. 3(a), the ordered magnetic moments of Mn^{2+} are 4.8(1) μ_B at 1.5 K.

In MnPrMnSbO$_6$, both Mn^{2+} and Pr^{3+} magnetic moments order along the z direction following Γ_1 of their respective IRs in Tables S4 and S6 and BV 3 of Γ_1 in Table S5 of the SM [27]. The resulting magnetic structure, depicted in Fig. 3(b), can be described as the AFM coupling between the FM Mn^{2+} sublattices and the FM aligned Pr^{3+} magnetic moments along the z axis. The maximum values of the magnetic moments reach 5.1(1) μ_B/Mn^{2+} and 2.2(1)μ_B/Pr^{3+}. The latter is in good agreement with the ~1.8 μ_B magnetization at saturation obtained in the hysteresis loop measured at 2 K (Fig. 1).

The thermal evolution of the magnetic moments in MnPrMnSbO$_6$ is depicted in Fig. 4. The progressive increase of both Pr^{3+} and Mn^{2+} magnetic moments, which order simultaneously at $T_N \approx 62$ K, confirms their collinear alignment along the z axis for the complete temperature range, in contrast to the spin-reorientation transition reported for the related MnNdMnSbO$_6$. The data have been fitted to the critical law $\mu(T) = \mu(0)[1 - (T/T_N)]^\beta$ in the temperature range $(T_N/2) < T < T_N$, shown as dashed red and black lines in Fig. 4 for Mn and Pr, respectively. The resulting β parameters, 0.36 and 0.37 for Mn^{2+} and Pr^{3+}, respectively, are in good

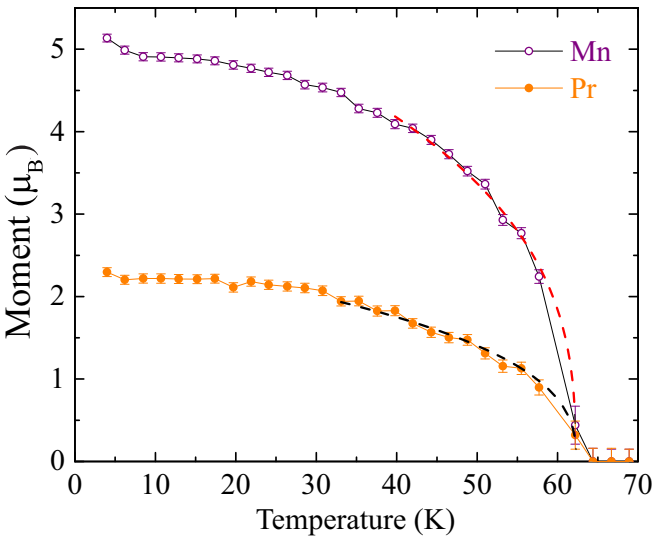

FIG. 4. Thermal evolution of the magnetic moments of Mn^{2+} (purple) and Pr^{3+} (orange) in $MnPrMnSbO_6$. The dashed red (Mn^{2+}) and black (Pr^{3+}) lines show the fits to the critical law $\mu(T) = \mu(0) * [1 - (T/T_N)]^{\beta}$.

agreement with the three-dimensional (3D) Heisenberg model, and the fitted T_N values, 62.2(2) and 62.3(3) K, respectively, demonstrate the simultaneous order of both sublattices.

B. Crystal-field parameters

As previously reported [19], the magnetic structure of $MnNdMnSbO_6$ below $T_{N1} \sim 76$ K can be described as the AFM coupling of the FM Mn^{2+} A and B sublattices ordered along the z axis [Fig. 3(c)]. Upon cooling the sample below $T_{N2} \sim 42$ K, the Nd^{3+} magnetic moments start to order, inducing a spin-reorientation transition of the Mn^{2+} spins, which ends with all the magnetic moments lying along the x axis. Similar magnetic behaviors are commonly observed among mixed transition-metal rare-earth compounds, which often include spin-reorientation transitions in the presence of Nd but not in that of Pr, e.g., in the $R_2Fe_{14}B$ permanent magnets [34]. This feature is commonly assigned to crystal-field-induced magnetic anisotropy [35].

According to Kramers theorem, the crystal field splits the ground term of a Nd^{3+} cation ($^4I_{9/2}$) into a doublet, while that of Pr^{3+} ($^3H_4$) is a singlet. We have estimated the CFPs for $4f^2$ and $4f^3$ configurations of Pr^{3+} and Nd^{3+} cations in $MnRMnSbO_6$ oxides using the semiempirical simple overlap model (see SM [27] for details) and considering the C_2 symmetry of their crystallographic position (4e Wyckoff) in the DDPv structure. The results are summarized in Table S1 in the SM [27]. The energy levels (Table S2 of the SM [27]) and their associated wave functions have been estimated by diagonalizing a Hamiltonian which includes these CFPs along with the FI contributions. By applying the magnetic dipole operator $L + g_e S$, which is represented by a first-rank tensor having three components that characterize the magnetic anisotropy, we calculated the temperature evolution of their paramagnetic susceptibilities (Fig. 5) according to the Van Vleck formalism. In the case of Nd^{3+} Kramers doublets, the g

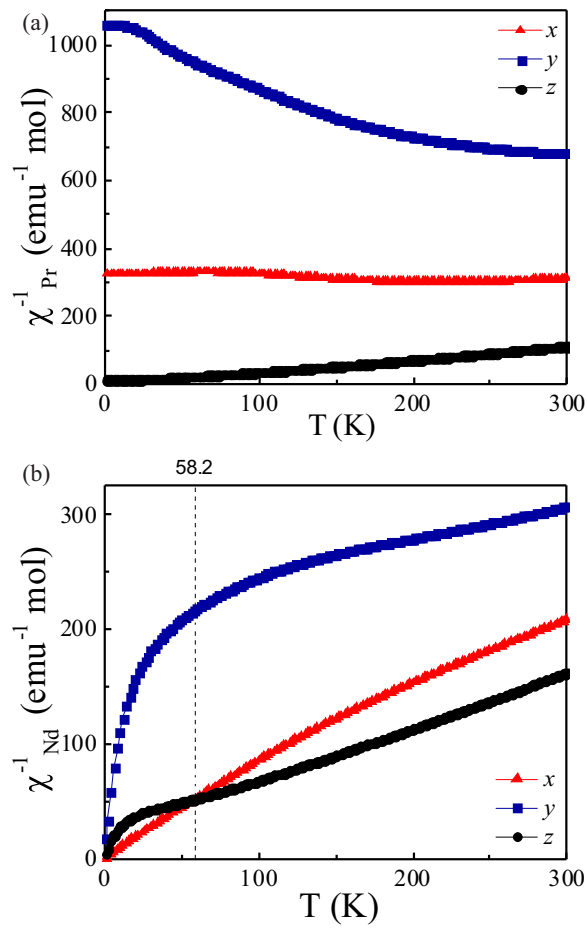

FIG. 5. Simulated reciprocal magnetic susceptibilities of (a) Pr^{3+} and (b) Nd^{3+} shown as independent components along the main crystallographic directions. The crossover temperature induced by the crystal field in Nd^{3+} (58.2 K) is marked with a line.

factors, shown in Table S2 of the SM [27], are also determined. Note the paramagnetic contributions depicted in Fig. 5 (direct values in Fig. SF1 of the SM [27]) are only arising from the R^{3+} cation and are not comparable in magnitude to the experimental values shown in Fig. 1, which also includes the Mn^{2+} sublattices.

From Fig. 5(a), the presence of a strong magnetic anisotropy is clear along the z direction for Pr^{3+}, as denoted by a dominant character of the z component for the studied temperature range. This anisotropy is in good agreement with the presence of the single (020) magnetic peak in the $3.85 < d < 4.05$ Å region of Fig. 2, with the magnetic structure determined from the NPD data and with its thermal evolution shown in Fig. 4. In contrast, both x and z components have comparable values at temperatures close to $T_{N1} \sim 76$ K in the Nd^{3+} compound. Thus, the magnetic structure is governed by the macroscopic negative Stevens coefficient (α_J) of the Nd^{3+} cations, which induces the alignment of the spins along the z axis [36] as it does for the related Pr^{3+} sample. However, below ~58 K [see Fig. 5(b)], the x component of the susceptibility overcomes that along the z direction, the reciprocal value becoming 0.25 times that of the z contribution at low temperatures due to the crystal-field effect. As a consequence, upon further cooling

the sample, this crystal-field-induced magnetic anisotropy overcomes the intrinsic one lead by the α_J coefficient. This results in the reported switch of the magnetic moments of $MnNdMnSbO_6$ at $T_{N2} \sim 42$ K [19]. Otherwise, in the absence of any crystal-field splitting of the singlet ground state of Pr^{3+} cations, the magnetic behavior of $MnPrMnSbO_6$ is governed by the intrinsic magnetic anisotropy of Pr^{3+} for the complete temperature range.

IV. CONCLUSIONS

The DDPv $MnRMnSbO_6$ oxides show collinear magnetic structures constituted of two FM sublattices at $Mn_{A/A'}$ and Mn_B (+ R for R = Pr, Nd) which are AFM coupled to each other. Three different types of magnetic anisotropic behaviors have been found in these compounds. $MnLaMnSbO_6$, with no paramagnetic R^{3+} cation, shows the intrinsic DDPv magnetic structure, where Mn^{2+} spins lie along the x axis. Otherwise, the magnetic anisotropy of Pr^{3+} and Nd^{3+} cations induces the order of the magnetic moments along z in $MnPrMnSbO_6$ and $MnNdMnSbO_6$. However, the separate order of Nd^{3+} moments induces a spin reorientation towards the x axis. We have calculated the energy levels of the ground term for both paramagnetic rare earths under their experimental point symmetries. The results reveal that the crystal-field-induced magnetic anisotropy overcomes the FI contribution in the case of Nd^{3+} due to the presence of Kramers doublets. As a consequence, $MnNdMnSbO_6$ exhibits a different, temperature-dependent, magnetic anisotropy.

ACKNOWLEDGMENTS

The authors thank EPSRC and the Royal Society for financial support. MINECO and Comunidad de Madrid are also acknowledged for funding through Projects No. MAT2013-44964, No. MAT2014-56607-R, and No. S-2013/MIT-2753, respectively. We thank the Institut Laue-Langevin for awarding beam time at the D20 instrument.

[1] M. R. Li, D. Walker, M. Retuerto, T. Sarkar, J. Hadermann, P.W. Stephens, M. Croft, A. Ignatov, C. P. Grams, J. Hemberger, I. Nowik, P. S. Halasyamani, T. T. Tran, S. Mukherjee, T. S. Dasgupta, and M. Greenblatt, Angew. Chem. Int. Ed. **52**, 8406 (2013).

[2] M. R. Li, M. Retuerto, D. Walker, T. Sarkar, P. W. Stephens, S. Mukherjee, T. S. Dasgupta, J. P. Hodges, M. Croft, C. P. Grams, J. Hemberger, J. Sánchez-Benítez, A. Huq, F. O. Saouma, J. I. Jang, and M. Greenblatt, Angew. Chem. Int. Ed. **53**, 10774 (2014).

[3] M. R. Li, M. Retuerto, P. W. Stephens, M. Croft, D. Sheptyakov, V. Pomjakushin, Z. Deng, H. Akamatsu, V. Gopalan, J. Sánchez-Benítez, F. O. Saouma, J. I. Jang, D. Walker, and M. Greenblatt, Angew. Chem. Int. Ed. **55**, 9862 (2016).

[4] M. R. Li, M. Croft, P. W. Stephens, M. Ye, D. Vanderbilt, M. Retuerto, Z. Deng, C. P. Grams, J. Hemberger, J. Hadermann, W. M. Li, C. Q. Jin, F. O. Saouma, J. I. Jang, H. Akamatsu, V. Gopalan, D. Walker, and M. Greenblatt, Adv. Mater. **27**, 2177 (2015).

[5] R. Mathieu, S. A. Ivanov, G. V. Bazuev, M. Hudl, P. Lazor, I. V. Solovyev, and P. Nordblad, Appl. Phys. Lett. **98**, 202505 (2011).

[6] A. J. Dos santos-García, E. Solana-Madruga, C. Ritter, D. Ávila-Brande, O. Fabelo, and R. Sáez-Puche, Dalton Trans. **44**, 10665 (2015).

[7] A. J. Dos santos-García, E. Solana-Madruga, C. Ritter, A. Andrada-Chacón, J. Sánchez-Benítez, F. J. Mompean, Mar Garcia-Hernandez, R. Sáez-Puche, and R. Schmidt, Angew. Chem. Int. Ed. **56**, 4438 (2017).

[8] M. R. Li, M. Retuerto, Z. Deng, P. W. Stephens, M. Croft, Q. Huang, H. Wu, X. Deng, G. Kotliar, J. Sánchez-Benítez, J. Hadermann, D. Walker, and M. Greenblatt, Angew. Chem. Int. Ed. **54**, 12069 (2015).

[9] A. M. Arévalo-López, G. M. McNally, and J. P. Attfield, Angew. Chem. Int. Ed. **54**, 12074 (2015).

[10] M. R. Li, J. P. Hodges, M. Retuerto, Z. Deng, P. W. Stephens, M. C. Croft, X. Deng, G. Kotliar, J. Sánchez-Benítez, D. Walker, and M. Greenblatt, Chem. Mater. **28**, 3148 (2016).

[11] A. M. Arévalo-López, F. Stegemann, and J. P. Attfield, Chem. Comm. **52**, 5558 (2016).

[12] G. V. Bazuev, B. G. Golovkin, N. V. Lukin, N. I. Kadyrova, and Yu. G. Zainulin, J. Solid State Chem. **124**, 333 (1996).

[13] A. J. Dos santos-García, C. Ritter, E. Solana-Madruga, and R. Sáez-Puche, J. Phys.: Condens. Matter **25**, 206004 (2013).

[14] R. Mathieu, S. A. Ivanov, I. V. Solovyev, G. V. Bazuev, P. Anil Kumar, P. Lazor, and P. Nordblad, Phys. Rev. B **87**, 014408 (2013).

[15] E. Solana-Madruga, A. J. Dos santos-García, A. M. Arévalo-López, D. Ávila-Brande, C. Ritter, J. P. Attfield, and R. Sáez-Puche, Dalton Trans. **44**, 20441 (2015).

[16] G. King and P. M. Woodward, J. Mater. Chem. **20**, 5785 (2010).

[17] G. King, S. Thimmaiah, A. Dwivedi, and P. M. Woodward, Chem. Mater. **19**, 6451 (2007).

[18] M.C. Knapp and P.M. Woodward. J. Solid State Chem. **179**, 1076 (2006).

[19] E. Solana-Madruga, Á. M. Arévalo-López, A. J. Dos Santos-García, E. Urones-Garrote, D. Ávila-Brande, R. Sáez-Puche, and J. P. Attfield, Angew. Chem. Int. Ed. **55**, 9340 (2016).

[20] J. M. D. Coey, Physica Scripta. **T19B**, 426 (1987).

[21] Y. Su, Y. Sui, J.-G. Cheng, J.-S. Zhou, X. Wang, Y. Wang, and J. B. Goodenough, Phys. Rev. B **87**, 195102 (2013).

[22] A. McDannald, L. Kuna, and M. Jain, J. Appl. Phys. **114**, 113904 (2013).

[23] J.-L. Jin, X. Q. Zhang, G.-K. Li, Z.-H. Cheng, L. Zheng, and Y. Lu, Phys. Rev. B **83**, 184431 (2011).

[24] J.-L. Jin, X. Q. Zhang, H. Ge, and Z.-H. Cheng, Phys. Rev. B **85**, 214426 (2012).

[25] R. Huang, S. Cao, W. Ren, S. Zhan, B. Kang, and J. Zhan, Appl. Phys. Lett. **103**, 162412 (2013)

[26] J. Rodríguez-Carvajal, *BasIreps: A Program for Calculating Irreducible Representation of Little Groups and Basis Functions of Polar and Axial Vector Properties*, Part of the FullProf Suite of programs, http://www.ill.eu/sites/fullprof/.

[27] See Supplemental Material at http://link.aps.org/supplemental/10.1103/PhysRevB.97.134408 for further explanations on the SOM calculations and magnetic symmetry analysis and supporting Figures and Tables.
[28] J. Rodriguez-Carvajal, Physica B **192**, 55 (1993).
[29] R. S. Puche, E. Climent, J. Romero de Paz, J. L. Martínez, M. A. Monge, and C. Cascales, Phys. Rev. B **71**, 024403 (2005)
[30] C. Zaldo, M. Rico, C. Cascales, M. C. Pujol, J. Massons, M. Aguiló, F. Díaz, and P. Porcher, J. Phys.: Condens. Matter **12**, 8531 (2000).
[31] C. Cascales, C. Zaldo, U. Caldiño, J. García Solé, and Z. D. Luo, J. Phys.: Condens. Matter **13**, 8071 (2001).
[32] P. Porcher, M. Couto dos Santos, and O. Malta, Phys. Chem. Chem. Phys. **1**, 397 (1999).
[33] P. Porcher, *Fortran Routines REEL and IMAGE for Simulation of d^N and f^N Configurations Involving Real and Complex Crystal Field Parameters* (1989).
[34] M. Sagawa, S. Hirosawa, H. Yamamoto, S. Fujimura, and Y. Matsuura, Jpn. J. Appl. Phys. **26**, 785 (1987).
[35] P. H. E. Meijer, Physica **26**, 61 (1960).
[36] R. Skomski and D. J. Sellmyer, J. Rare Earths, **27**, 675 (2009).